



Properties of cobalt-doped SrTiO₃ derived from two methods: the modified Pechini method and the citrate combustion method

Adrian Mizera¹ · Ewa Drożdż¹

Received: 9 December 2022 / Accepted: 12 July 2023 / Published online: 19 August 2023
© The Author(s) 2023

Abstract

Two wet-synthesis methods: citrate-combustion and modified (with PVA addition) Pechini synthesis were used to obtain Co-doped strontium titanate with assumed chemical compositions of SrTi_{1-x}Co_xO₃ (where x = 0.02; 0.06; 0.10). All samples were calcined at 900 °C and sintered at 1200 °C, with PVA series being also calcined at 700 and 800 °C, since TG measurements indicated for this method materials lower minimal calcination temperature than for the citrate-combustion series materials. In general, the modified Pechini approach lowers calcination temperature of materials (up to 200 °C) and produces more structurally homogeneous materials than in the case of the citrate-combustion methods. However, the HT XRD measurements reveal the presence of extra cobalt oxide phases in pva_STO_xCo materials that were not visible using conventional XRD measurements. The presence of cobalt oxide has been confirmed for both series of materials based on TPR tests. Moreover, these measurements indicate the incorporation of some amount of cobalt into the perovskite structure. The fact of substituting titanium with cobalt in SrTiO₃ structure seems to be confirmed by the results of XAS studies. Additionally, XAS results allowed us to state that Co²⁺/Co³⁺ ratio fell as cobalt loading increased in the materials. The examination of SrTiO₃ lattice parameter changes for sintered samples is consistent with the findings of the XAS tests and indicates that cobalt adopts +2 oxidation state in the case of the material with the lowest Co content, and the share of Co³⁺ increases with the growth of the Co amount introduced into the system.

Keywords Co-doped SrTiO₃ · Wet synthesis methods · Co oxidation states · Cobalt oxides · Reduction · Perovskite · Catalyst

Introduction

Mixed-cation oxide ceramic materials play an important role in the fabrication of a wide range of devices, including transistors or capacitors for electronic applications, lead-zirconia ceramics for piezoelectric applications, and high-temperature superconductors. Besides bulk uses, highly porous mixed oxides are also employed as electrodes in solid oxide fuel or electrolysis cells, catalytic and photocatalytic applications, and lithium ion battery technologies. SrTiO₃ is a perovskite material with a cubic structure that, like other perovskites, can be easily doped in both the Sr and Ti locations, altering its properties significantly [1]. Doping the SrTiO₃ structure at the Ti position with aliovalent elements

can enhance the formation of oxygen vacancies in such a material, transforming it into a mixed ion–electron conductor. The use of a catalytically active admixture ingredient may also increase the overall catalytic activity of a material. Cobalt-doped SrTiO₃ is an example of the perovskite mixed oxide material that has already been studied for use in catalysis [2, 3]. The literature data covers the investigation of the magnetic properties [4–9], electrical conductivity [10, 11], photocatalytic properties [12], the measurements of the oxygen storage capability [13], and also catalytic reactions towards CO oxidation and NO reduction with CO [14]. Also, computational methods were employed by Carlotto et al. to investigate the catalytic properties of Co-doped SrTiO₃ [15, 16]. In the field of heterogenous catalysis, a high specific surface area is one of the most crucial requirements for the materials. In the case of metal oxide materials, two approaches to producing homogeneous mixed oxide materials with high porosity can be distinguished. The representative of the first group is a solid-phase reaction method.

✉ Adrian Mizera
amizera@agh.edu.pl

¹ Faculty of Materials Science and Ceramics, AGH University of Krakow, Kraków, Poland

Despite its simplicity, possible contamination, e.g., milling, may disqualify the method in the case of producing materials with a precise chemical composition. High calcination temperatures can also lead to uncontrollable grain growth. Another group of methods—wet chemical synthesis methods—has the advantage of greater control over the mentioned grain size and shape. These methods often employ the chemical properties of a single atom or molecule to self-organise or self-assemble into desired conformations, which influence the final material homogeneity and/or microstructure [17, 18]. However, most of the publications describing SrTiO₃-based materials obtained by these methods usually state that, apart from the perovskite phase, other phases are present in the materials, such as R–P (Ruddlesden–Popper) phases, SrCO₃, or cobalt oxides. In this paper, we focused on two sol–gel synthesis methods: citrate combustion and the Pechini method, which are often employed to synthesise a wide range of mixed-oxide materials. The sol–gel process allows for the formation of oxide nanomaterials by hydrolysis of metal alkoxides that form a sol and then gel through condensation of the hydrolysis products (condensation) to form an oxide network, and the sol is transformed into a gel and dried gel after solvent evaporation. Dried gel is transformed into an oxide during calcination, removing all organic residue. In the case of the sol–gel methods, the production of the oxide nanopowders has to be preceded by an adjustment of the synthesis conditions, especially when producing mixed-cation oxides. In the classic sol–gel synthesis, the alkoxides are used as a source of metal (or non-metal) cations. There are also a few methods involving the combustion of various organic molecules used as “fuel”. For instance, one synthesis involves heating the metal nitrates with urea and can proceed explosively. In the previously mentioned citrate-combustion method, citric acid is used as a complexing agent and as a “fuel”. In this case, the metal nitrates are mixed with citric acid in an aqueous environment, and the resulting mixture is stirred until a clear solution containing metal-citrate complexes is obtained. Further heat treatment leads to the evaporation of solvents, the thermal decomposition of the citrates, the oxidation of organic residues, and finally the formation of mixed oxide. The combustion of the organic residue takes place not only by the reaction with oxygen from the atmosphere but also by the reaction with nitrates present in the mixture. Metal alkoxides can also be used as substrates in the synthesis, resulting in the combination of the sol–gel process and the combustion of the organic matrix. This method is also known as the citrate sol–gel method. Although such a procedure is often used for the synthesis of mixed oxides [19, 20], it has some limitations [2]. When multi-cation oxides are synthesized, the hydrolysis and condensation reaction kinetic differences for each cation can lead to the precipitation of, e.g., metal hydroxides as separate phases. Combined with the possible

precipitation of the metal citrates, it leads to a decrease in the homogeneity of the mixture and the presence of multiple oxide phases rather than a single mixed oxide in the final material. The Pechini process is frequently used as an example of a procedure that allows for the synthesis of homogeneous and single-phase mixed oxides containing multiple metal cations [21–23]. The Pechini synthesis starts with the mixing of metal salts with the α -hydroxycarboxylic acid (such as citric acid) to form a clear solution with metal-citrate complexes. In the next step, the polyhydroxy alcohol (e.g., ethylene glycol) is added, and the mixture is stirred with heating. At this point, all the metals should be well mixed on a molecular level. The heating induces the polyesterification reaction to occur between the polyhydroxy alcohol and the metal-citrate complexes. Chelation and subsequent polymerization of the metal chelates immobilise the metal cations in a cross-linked resin [24]. The immobilisation of the metal cation is even increased due to the evaporation of the solvents. A similar effect occurs in another synthesis technique—organic steric entrapment synthesis. In this method, most frequently, water-soluble polymers are mixed with the nitrate solutions, the mixture is heated to remove water, and the metal ions become entrapped in the polymer resin. Steric entrapment of the metal cations keeps them from taking part in the hydrolysis reaction. This is one of the possible reasons why the oxides can separate in citrate-combustion synthesis, which is not the case in the Pechini process [25–28], where if all preceding steps are done correctly, the water is removed during heating and after the stable polymer network of metal chelates is formed, preventing the metal cations from undergoing hydrolysis reactions. Calcination of the dried resin in the temperature range of 500–900 °C leads to oxidation of the organics and results in the formation of the final mixed-cation oxide material. The organic (polyhydroxy alcohol and citric acid) content in a synthesis can vary, which also has an influence on the required calcination temperature—the samples prepared with low organic content should have a lower calcination temperature, which is important in the case of catalyst material production.

In both methods, there is the possibility of tuning the ions/citric acid ratio or changing the pH of the solution [29]. Also, additives such as surfactants can be added [30, 31]. Moreover, in the Pechini method, the polyhydroxy alcohol can be substituted by a polymer with OH groups, such as poly(vinyl alcohol), as we did in the presented work.

The goal of our work was to compare the properties of the materials synthesized via two different methods: the citrate-combustion (or citrate sol–gel) method and the modified Pechini method. In both series of materials, samples with nominal cobalt contents of 2, 6, and 10 mol. % (in relation to Ti) were obtained. The modification of the Pechini method was done by replacing the polyhydroxy alcohol with a water-soluble polymer—poly(vinyl alcohol) (PVA). We

studied the structure of the obtained powders (XRD, high temperature XRD, and XAS measurements for confirmation of titanium and cobalt oxidation states), observed the microstructure under the SEM microscope, and investigated the redox (TPR/TPOx) properties of both series of materials.

Methods

The phase composition of calcined and sintered materials was determined on the basis of diffractograms, which were obtained using the X-ray diffractometer Panalytical X'Pert Pro MD equipped with CuK α radiation source ($\lambda = 1.5406$ Å) in the range of 2θ angle from 10° to 90° . Registered diffractograms were analysed in HighScore Plus software to identify crystal phases and determine their amounts by Rietveld refinement. The average crystallite size was calculated from the full width at half maximum of XRD reflections by using the Scherrer formula.

Moreover, XRD measurements as a function of temperature (HT_XRD) were also performed for pva_STO_6Co and pva_STO_10Co samples. This type of measurement was conducted using a PANalytical Empyrean diffractometer in Bragg–Brentano geometry in the air atmosphere. The samples selected for these measurements were prepared in the following way: the precursor powders dried at 200°C overnight were pre-heated at 500°C for 1 h in the air atmosphere to remove nitrates and some of the organic residue from the samples. After cooling, the powders were crushed in an agate mortar and shaped into cylindrical pellets. In such a form, the samples were tested as described below. The X-ray beam was produced with a copper lamp, and the radiation wavelengths were: CuK $\alpha_1 = 1.5406$ Å and CuK $\alpha_2 = 1.54443$ Å. The radiation was filtered using a nickel filter. The measurements were made in the angular range 2θ from 10° to 90° and in the temperature range 300 – 1100°C with a scan every 100°C . The heating rate was set to 5°C min^{-1} and before each scan, the temperature of the sample was stabilised for 30 min. The additional scans were taken before starting the heating and after completing the entire series of measurements at high temperatures (after cooling the sample to RT for c.a. 3 h).

X-ray absorption spectroscopy (XAS) measurements were carried out on the PIRX beamline in the Solaris infrastructure with the use of the SDD fluorescent Amptek detector (total (TFY) and partial (PFY) fluorescence modes). The measurements were performed for pva_STO_xCo powder materials for the determination of Co and Ti oxidation states. Excluding the CoO reference, all spectra were registered using the SDD detector in fluorescence mode. The CoO reference spectra were registered in the total electric yield mode (TEY) by measuring the cobalt(II) oxide sample already available in the SOLARIS facility in the experiment

line. All spectra were acquired at room temperature. The powder samples were pressed into a carbon sheet (compatible with ultra-high vacuum) and mounted to typical titanium flag-style Omicron holders to provide conductivity and hence protection from X-ray-induced charge.

The calcination temperature of materials was determined on the basis of thermogravimetry measurements (TG method) using the NETZSCH STA 449 F3 apparatus. The measurements were performed with a heating rate of $10^\circ\text{C min}^{-1}$ in the flow of air.

SEM microphotographs were obtained using scanning electron microscopy provided by Nova NanoSEM 200 FEI.

Temperature-programmed reduction and oxidation (TPR and TPOx) measurements were carried out using the Chem-iSorb 2750 apparatus by Micromeritics. The following gas mixtures were used (in vol%): TPR—5% H₂/Ar, TPOx—5% O₂/Ar at a flow rate of 40 mL min^{-1} . For each experiment, a similar mass of the sample was used (approximately 0.2 g). Each sample was tested in the temperature range from RT to 900°C in the following way: the first cycle of the reduction (I TPR), the first cycle of the oxidation (I TPOx) and the second cycle of the reduction (II TPR), with cooling in a helium atmosphere between the cycles.

Synthesis

The materials with the general formula SrTi_{1-x}Co_xO₃ (where $x = 0.02; 0.06; 0.10$) were prepared using two wet chemical methods: the citrate-combustion method (labelled as cit_STO_2Co, etc.) and the modified Pechini method (labelled as pva_STO_2Co, etc.). All materials were prepared using analytical grade reagents. Both syntheses started with the dissolution of half the amount of citric acid in methanol (Avantor) with constant stirring and heating at 50°C . The molar ratio of citric acid (monohydrate; Avantor) to the sum of moles of Sr, Ti, and Co was set at 3:2. After 10 min of stirring and heating, titanium (IV) isopropoxide (Arcos Organics) was added to the solution, resulting in the formation of a white precipitate, followed by the addition of the remaining half amount of citric acid. The volumetric ratio of methanol used in syntheses to the titanium (IV) isopropoxide was adjusted at 5:1. After dissolving the precipitate, a clear straw-coloured solution was obtained, to which appropriate volumes of Sr(NO₃)₂ (Arcos Organics) and Co(NO₃)₂ (Avantor) aqueous solutions (with a concentration of about 1.5 and 1.0 mol dm^{-3} , respectively) were added. In the case of citrate-combustion synthesis, the resulting clear solution was heated at 120°C for 3 h and then at 200°C overnight. The second method—the modified Pechini method—is similar to the point where the strontium and cobalt nitrate solutions are added to the mixture. The modification of the classical Pechini approach consisted of replacing the polyhydroxy

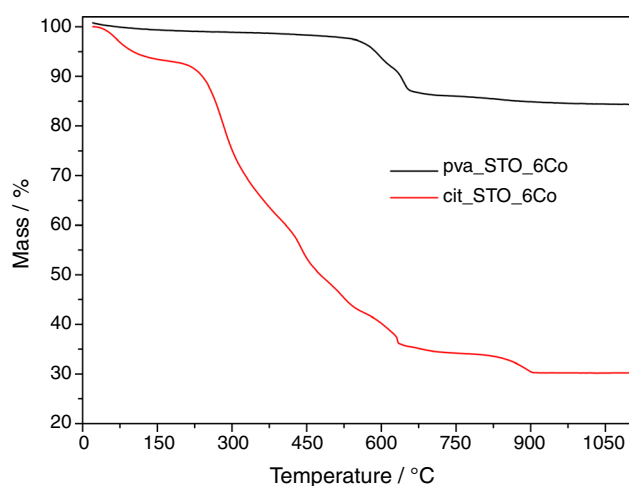


Fig. 1 TG curves of Co-doped SrTiO₃ dried precursor

alcohol with a polymer containing OH groups—poly(vinyl alcohol)—PVA (Avantor). After a couple of minutes of stirring, the heating was turned off to cool the mixture to room temperature. After cooling, the previously prepared 8% aqueous solution of PVA was introduced to the mixture and stirred for 15 min. After that time, the heating was turned on again and set at 120 °C for 3 h to induce the formation of resin. Analogous to the citrate-combustion method, the samples were dried at 200 °C overnight. Before proper calcination, the dried materials were crushed and ground in an agate mortar. All samples were calcined at 700, 800, and 900 °C for 3 h in the air atmosphere, reaching the calcination temperature with a heating rate of 1 °C min⁻¹.

Results and discussion

One of the basic assumptions related to the use of two wet synthesis methods was to obtain single-phase materials using the lowest possible temperatures. Thus, to determine the proper calcination temperature of the two series of materials, the thermal analysis method (TG) was used. In our manuscript, we assume that the calcination temperature is the temperature after which the mass loss of the sample is negligible (< 1%). Figure 1 shows the TG curves of STO_6Co materials after overnight drying at 200 °C (in the case of citrate-combustion synthesis) and after overnight drying at 200 °C and initial heating at 400 °C for 1 h (in the case of modified Pechini synthesis). Because citric acid decomposes at around 200 °C [32] and PVA decomposes at 330 °C (the major effect) [33], such thermal treatment was used to remove some of the organic residues: citric acid and PVA before proper TG measurement. The main mass loss in materials after PVA method synthesis occurs at around 600 °C and is associated with the oxidation of the majority

of the organic part of the sample. Above that temperature, only a slight mass loss can be observed, which may be associated with the decomposition of the traces of SrCO₃, decomposition of Co₃O₄ (mostly around 900 °C), or the formation of oxygen vacancies and thus the release of oxygen from the perovskite crystal lattice. It is possible that all of these processes take place, however, these processes are not significant considering that in the temperature range of 700–900 °C mass changes are of the order of 1 mass%. Several stages of mass loss can be distinguished in the case of citrate synthesis. Water evaporation and the decomposition or combustion of perovskite precursors are among the processes that occur at temperatures below 600 °C in this type of perovskite material synthesis [31]. The final mass loss corresponding to the decomposition of SrCO₃ [34] occurs around 900 °C. The presence of strontium carbonate phase was observed only in cit_STO_xCo materials, and the results of diffraction measurements presented in the further part of the manuscript confirm this fact. Given these results, we assumed that the minimal calcination temperature is 700 °C for materials synthesized using the modified Pechini method and 900 °C for materials obtained from the citrate method. Due to such large differences in calcination temperatures determined on the basis of TG curves (200 °C), the materials obtained by the Pechini method were also calcined at an intermediate temperature (800 °C) and at the same temperature as for the citrate combustion series (900 °C).

To confirm the correctness of the selection of the calcination temperature and to examine the phase composition of the obtained materials, X-ray diffraction (XRD) tests of materials after calcination were carried out. The phase composition of the synthesized materials differs depending on the synthesis route (Fig. 2). In all samples produced via the modified Pechini method, only the tausonite crystal phase is present (SrTiO₃, ICDD no. 98-002-3076), while materials obtained from citrate-combustion synthesis are multiphase, and, in addition to SrTiO₃, the Ruddlesden-Popper phases (Sr₂TiO₄, ICDD no. 98-015-7402 and Sr₄Ti₃O₁₀, ICDD no. 98-003-4630), rutile (TiO₂, ICDD no. 98-006-2679) and strontianite (SrCO₃, ICDD no. 98-020-2793) were identified. XRD analysis does not confirm any of the possible cobalt oxides (CoO, CoO_{1+x}, Co₃O₄, Co₂O₃ or CoO₂) as separate phases for any of the series of materials. The phase composition of the materials from both synthesis methods is shown in Table 1 (samples from citrate synthesis) and in Table 2 (samples from synthesis with PVA). Additionally, the mean crystallite size of tausonite phases based on the half-width of the diffraction peaks was calculated for both series and placed in these tables.

The results shown in Fig. 2a confirmed that a minimum calcination temperature of 700 °C was sufficient to obtain single-phase materials from the modified Pechini synthesis, as only diffraction patterns for tausonite are visible. The

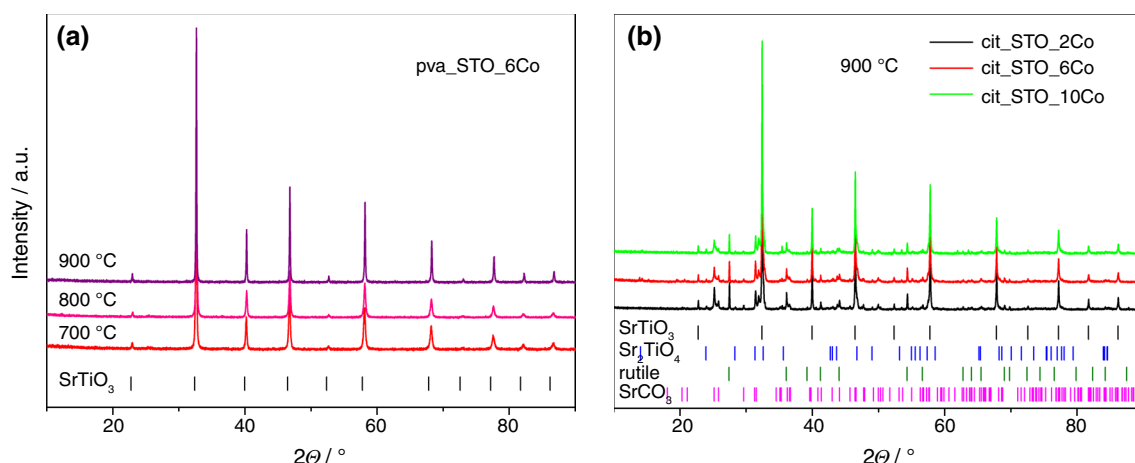


Fig. 2 X-ray diffraction patterns of Co-doped strontium titanates obtained from **a** the modified Pechini method and **b** citrate combustion method

Table 1 The phase composition of the samples from citrate-combustion synthesis calcined at 900 °C and the mean crystallite size of tausonite phase

Sample/crystal phase	Tau-sonite/mas. %	Tausonite mean crystallite size/nm	Rutile/mas. %	Strontian-ite/mas. %	Sr ₂ TiO ₄ + Sr ₄ Ti ₃ O ₁₀ (R-P)/mas. %
cit_STO_2Co 900 °C	61.1	176 ± 12	12.9	8.1	18.0
cit_STO_6Co 900 °C	61.3	169 ± 14	11.3	5.9	21.6
cit_STO_10Co 900 °C	62.0	183 ± 15	9.6	6.0	22.4

Table 2 The mean crystallite size of the tausonite phase for samples obtained from the synthesis with PVA and calcined at different temperatures

Mean crystallite size of tausonite phase/nm			
Sample/calcination temperature	700 °C	800 °C	900 °C
pva_STO_2Co	34 ± 8	44 ± 8	122 ± 10
pva_STO_6Co	28 ± 5	37 ± 8	99 ± 12
pva_STO_10Co	36 ± 9	46 ± 10	113 ± 10

samples calcined at 800 °C and 900 °C had the same phase composition. It is worth noting that the XRD method used for phase identification has a limited sensitivity—crystalline phases below 1% may not be detected in the diffraction patterns. Thus, other phases (aside from SrTiO₃) may be present in a material in very small quantities, particularly if they are partially or entirely amorphous.

In the case of samples derived from the citrate method (Fig. 2b), one of the crystalline phases present is strontium carbonate, the presence of which may result from one of two sources: the first one is that SrCO₃ is formed as a secondary reaction product ($\text{SrO} + \text{CO}_2 \rightarrow \text{SrCO}_3$) and the second one

is that SrCO₃ was formed in the first step of synthesis and has not completely decomposed at 900 °C. In addition, the presence of multiple crystalline phases may result from the separation of ions during powder synthesis. In the citrate method, citric acid acts as a complexing agent for ions present in the solution (a mixture of precursors). However, it is possible that the complexation is incomplete, and some of the ions in the solution may precipitate as hydroxides or salts, reducing the degree of homogeneity of such a system. The presence of strontium carbonate may be due to the fact that a certain amount of strontium is not present in the complex compounds formed with citric acid, resulting in strontium oxide segregation. Consequently, during calcination, SrO binds with CO₂ to form the phase SrCO₃, which has a high temperature of thermal decomposition. Other crystal phases, such as rutile and Ruddlesden–Popper phases, are then formed as the ratio of strontium to the other ions is disrupted by the formation of strontium carbonate.

Furthermore, the sizes of the tausonite phase crystallites (calculated using diffraction data) were compared for both series of materials (Tables 1 and 2). One can observe that there is no correlation between the amount of cobalt and the average crystallite size of the tausonite phase for materials derived from both, the modified Pechini and citrate methods.

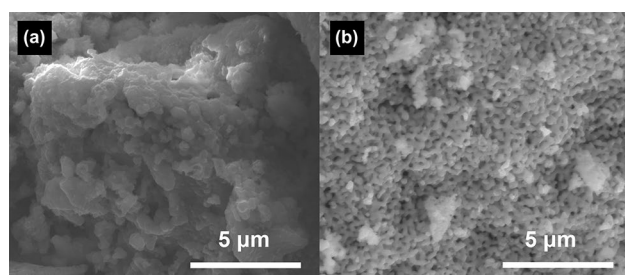


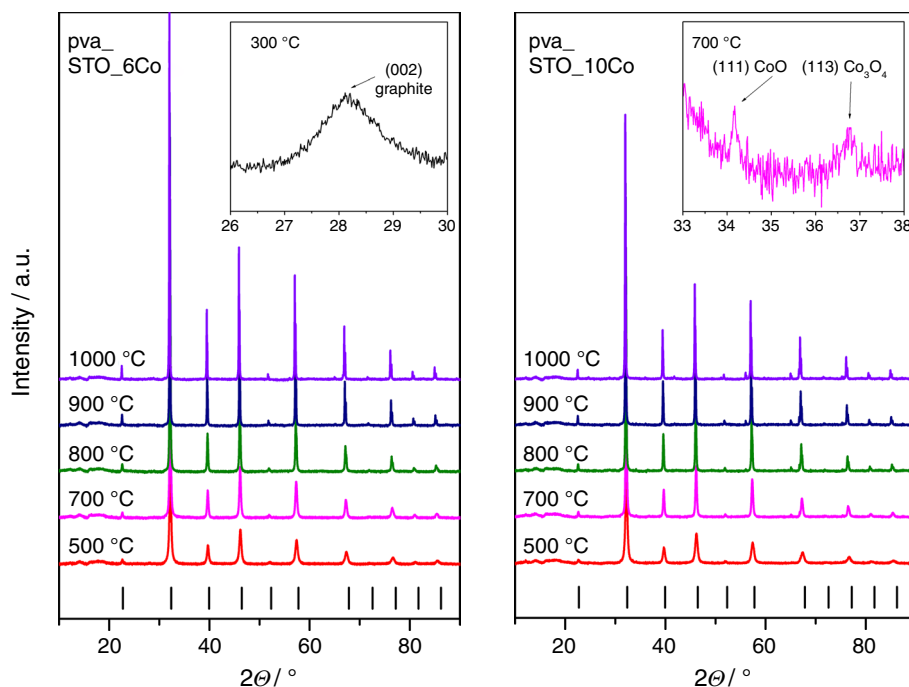
Fig. 3 SEM images of **a** cit_STO_6Co and **b** pva_STO_6Co materials after calcination at 900 °C

Moreover, in the case of the PVA method, an increase in the mean crystallite size of the SrTiO_3 phase with increasing calcination temperature is observed. In particular, when comparing the materials after calcination at 900 °C, it can be noticed that the samples from the citrate method consist of crystallites much larger than those of the PVA series. The microstructure of powder samples (Fig. 3) shows that both series' materials are made up of grain agglomerates. The mean grain sizes for both material series (900 °C), those produced by the citrate method and those produced by the PVA method, are 176 ± 14 nm and 111 ± 11 nm, respectively.

The XRD and SEM analyses show that the materials with the pva_STO_xCo series have much greater homogeneity, both in terms of phase composition and microstructure, than the materials with the cit_STO_xCo series. However, the results of temperature-programmed reduction of materials (performed for both series) presented in the further part of the manuscript did not confirm this homogeneity (in terms of phase) of materials in the case of the pva_STO_xCo series. Therefore, it was decided to conduct a more detailed study on the possibility of creating various phases during thermal treatment of pva_STO_xCo series materials. Thus, diffractometric measurements as a function of temperature (HT XRD) were performed and analysed for pva_STO_6Co and pva_STO_10Co samples during heating in an air atmosphere at the temperature range 25–1100 °C (Fig. 4). The tests for the pva_STO_2Co material were not performed due to the small amount of cobalt introduced into the system, resulting in high uncertainty in determining the presence and, even more so, the amount of Co-related phases. The materials used in HT XRD analysis were only preheated to 500 °C (they were not calcined at higher temperatures), as mentioned in *Experimental*, so that the sequence of processes and phases formed during further thermal treatment could be observed. The preliminary thermal treatment was, however, necessary due to the large amounts of organic and nitrate precursors contained in the material, which was heated only in an oven at 200 °C. The initial composition of the tested samples (Table 3) reveals that the materials (previously heated to 500 °C) contain tausonite as the main

phase, a large amount of carbon, and, in the case of one of the pva_STO_6Co samples, TiO_2 . The presence of carbon in samples indicates that the organic residue was not completely burned, whereas the presence of TiO_2 indicates that 500 °C was too low temperature for a complete reaction or that the material's residence time at this temperature was too short. Due to the difficulties in the Rietveld analysis for the sample pva_STO_6Co heated at 300 °C, we decided to show only the results of the HT XRD experiment room temperature (RT) measurement and measurements from temperatures equal to or higher than 400 °C. The presence of crystalline TiO_2 proves that at least part of the titanium introduced into the system first changes into the oxide form, and only higher temperatures or longer reaction times due to ion diffusion lead to the incorporation of all titanium into the perovskite structure. Moreover, the diffraction patterns for these samples have a very high background, especially in the low-angle range, indicating the presence of amorphous phases. It can, therefore, be assumed that both strontium and cobalt may be partially present in the materials in the form of amorphous oxides. The analysis of diffractograms for materials heated in the HT XRD apparatus up to 400 °C does not indicate qualitative changes, but there are quantitative changes (the amount of carbon is slightly reduced) in the system. Tausonite is the only phase present in the pva_STO_6Co material at 500 °C. This demonstrates that when the temperature is raised to this level again, TiO_2 completely reacts with amorphous SrO to form the SrTiO_3 system. Thus, in both the citric acid method and the modified Pechini method, the formation of TiO_2 and its subsequent reaction with SrO may be an intermediate step in the formation of tausonite. Surprisingly, the R-P phases (enriched with strontium compared to the tausonite phase) are not formed in the PVA method, whereas they are present in the cit_STO_xCo materials. As a result, it appears that the presence of poly(vinyl alcohol) causes the release of strontium oxide in amorphous form, whereas when it is absent, strontium is bound as Sr_2TiO_4 or possibly other R-P phases that we have previously observed [2]. Carbon residues are still present at 500 °C in the pva_STO_10Co material, in addition to SrTiO_3 . At 600 °C, traces of cobalt(II) oxide become visible for the pva_STO_10Co sample, and at 700 °C, the Co_3O_4 phase appears. The cobalt oxide phases in the pva_STO_6Co sample are not visible until temperatures reach 900 °C.

However, until 900 °C, a similar phase composition is observed in the case of the pva_STO_6Co material. The literature data [35, 36] present both, the considerations and the phase diagram of the Co–O system, which states that the presence of CoO and Co_3O_4 at a given temperature is a function of O_2 pressure. At a partial pressure of oxygen of 0.2 atm, thermogravimetric measurements show that cobalt(II,III) oxide decomposes into cobalt(II) oxide at a temperature of about 900 °C according to the equation

Fig. 4 HT_XRD diffractograms of pva_STO_6Co and pva_STO_10Co samples

$\text{Co}_3\text{O}_4 \rightarrow 3\text{CoO} + \frac{1}{2} \text{O}_2$. These considerations are consistent with our observations because, as the temperature rises further, the amount of Co_3O_4 decreases and the share of

Table 3 The results of Rietveld analysis for HT_XRD measurements of pva_STO_xCo series

Temperature/°C	Phase composition/mas. %			
	pva_STO_6Co		pva_STO_10Co	
RT	SrTiO ₃	55.6	SrTiO ₃	72.6
	C	34.4	C	27.4
	TiO ₂	10.0		
400	SrTiO ₃	62.2	SrTiO ₃	91.8
	C	33.7	C	8.2
	TiO ₂	4.1		
500	SrTiO ₃	100	SrTiO ₃	93.6
			C	6.4
600	SrTiO ₃	100	SrTiO ₃	98.8
			CoO	0.2
700	SrTiO ₃	100	SrTiO ₃	98.0
			Co ₃ O ₄	2.0
800	SrTiO ₃	100	SrTiO ₃	98.3
			CoO	0.3
			Co ₃ O ₄	1.4
900	SrTiO ₃	98.2	SrTiO ₃	99.0
	CoO	0.1	CoO	0.3
	Co ₃ O ₄	1.7	Co ₃ O ₄	0.7
1000	SrTiO ₃	97.6	SrTiO ₃	99.1
	CoO	0.9	CoO	0.5
	Co ₃ O ₄	1.5	Co ₃ O ₄	0.4
1100	SrTiO ₃	98.5	SrTiO ₃	99.8
	CoO	0.9	CoO	0.2
	Co ₃ O ₄	0.6		

CoO increases in the tested systems. As mentioned earlier, with regard to the results of thermogravimetric measurements, the effect caused by the release of oxygen when Co_3O_4 breaks down is demonstrated by a slow decrease in mass on the TG curve for the pva_STO_6Co sample (see Fig. 1). It should be added that the differences in the phase composition analysis verified by HT HRD measurements and the composition given for materials calcined at 900 °C are the result of diametrical differences in the thermal treatment of materials subjected to both measurements. The calcined materials were kept at 900 °C for 3 h to allow the solid phase reaction processes to complete. Importantly, the HT XRD test indicated that, in this case (compared to the citrate method of synthesis), the formation of TiO₂ is an intermediate step, but no R-P phase is formed.

To confirm the presence of cobalt in various oxidation states (whether in the form of oxides or incorporated into the perovskite structure), X-ray absorption spectroscopy studies were carried out. Figures 5 and 6 show the normalized $L_{3,2}$ edges of XANES spectra registered for titanium and cobalt, respectively, in the materials obtained by synthesis with PVA and calcined at 700 °C (solid lines). Dashed lines represent the spectra registered for the reference oxide materials (CoO, Co_3O_4 , and rutile TiO₂). The spectra were normalized to the same height in the edge absorption energy (E_0). The pre-edge line was determined from the extrapolation of the measurement points from the energy range 8–18 eV before the $E_{0,\text{Co}} = 778.2$ eV for cobalt scans, and the energy range 6–20 eV before the $E_{0,\text{Ti}} = 457.8$ eV for titanium scans. The post-edge lines were determined from the

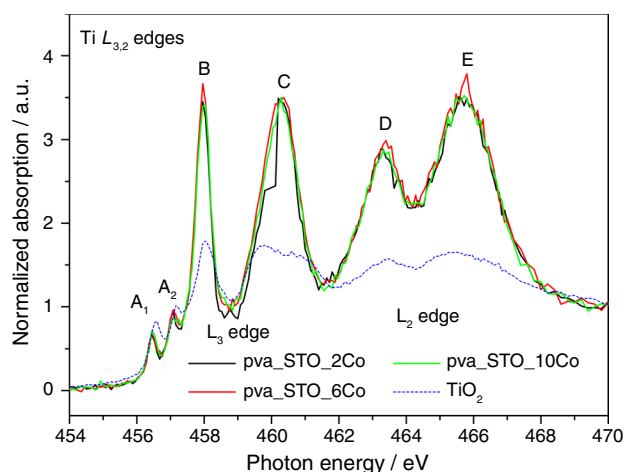


Fig. 5 Normalized Ti $L_{3,2}$ XANES spectra for pva_STO_xCo samples calcined at 700 °C and the normalized spectrum of reference TiO_2 oxide (dashed line)

measurement points above the L_2 edge. For cobalt scans, the post-edge lines were determined on the basis of the measurement points in the range of 22–70 eV above the $E_{0,\text{Co}}$ and for titanium scans, this range was in the energies of 12–60 eV above the $E_{0,\text{Ti}}$. The shape of the L edges results from the local electronic structure of the metal ion and provides information on, e.g., the valence state or the symmetry of the ground state. In our experiment, we measured the X-ray absorptions corresponding to the electron transitions from the core $2p_{1/2}$ (L_2 edge) and the $2p_{3/2}$ (L_3 edge) levels to the $3d$ levels.

Figure 5 shows the normalized spectra of perovskite samples and the reference TiO_2 (rutile) sample. Several features can be seen in the perovskite and rutile samples, including the pre-edge peaks labelled A_1 and A_2 .

These pre-peaks are typical for $3d^0$ compounds (unoccupied d orbitals) emerging from dipolar forbidden transitions [37, 38]. Another set of L_3 -edge and L_2 -edge absorption peaks is labelled as B ($E=458$ eV), C ($E=460.2$ eV), D ($E=463.4$ eV) and E ($E=465.8$ eV) corresponding to the transitions of $2p_{3/2}$ to T_{2g} , $2p_{3/2}$ to e_g , $2p_{1/2}$ to T_{2g} and $2p_{1/2}$ to e_g , respectively. The shape of the rutile spectrum is generally similar to those registered for pva_STO_2, 6 and 10Co samples, indicating the titanium oxidation state as Ti^{+4} . However, the spectra for the doped strontium titanates are shifted towards lower energies (about 0.2 eV), which is more pronounced in the pre-edge and rising edge regions. Such a shift is generally a sign of a change in the oxidation state towards a lower oxidation state. The effect is, however, small, indicating the limited reduction of Ti^{4+} to Ti^{3+} . It is worth noting that the reduction of titanium in the doped perovskite system can occur as a compensation mechanism of the perovskite lattice when an admixture element with a lower oxidation state is incorporated into the structure.

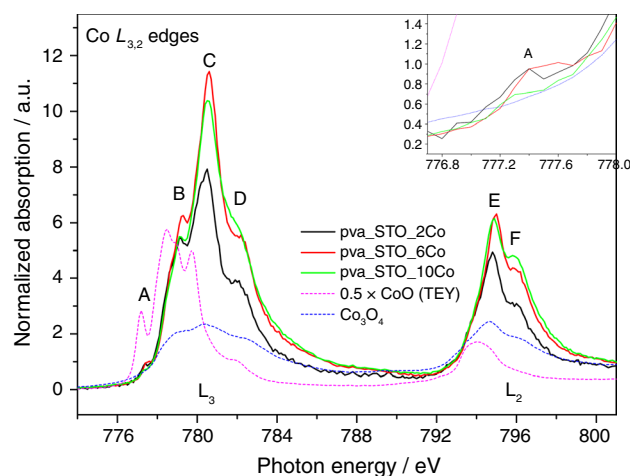


Fig. 6 Normalized Co $L_{3,2}$ XANES spectra for pva_STO_xCo samples calcined at 700 °C and the normalized spectra of reference CoO and Co_3O_4 oxides (dashed line). The CoO oxide was measured in the total electric yield mode and the intensity of the signal was divided by 2

Neglecting the electron–electron interaction, the intensity ratios of these peaks should be $I(B):I(C):I(D):I(E)=6:4:3:2$, but this is not the case in our work. In our case, the multiplet features are complicated and are the results of the combination of different covalent effects and Coulomb interactions (mentioned above) [37, 39]. In the case of the C absorption peak, the dropdown in the range 459.8–460.2 eV is most likely a result of the beam damage during the experiment.

In the case of the cobalt XANES experiment (Fig. 6), the L_3 -edge and L_2 -edge absorption peaks are labelled as A ($E=777.4$ eV), B ($E=779.3$ eV), C ($E=780.5$ eV), D ($E=782.2$ eV), E ($E=794.9$ eV), and F ($E=796.0$ eV), corresponding to the transitions of $2p_{3/2}$ to T_{2g} , $2p_{3/2}$ to e_g , $2p_{1/2}$ to T_{2g} and $2p_{1/2}$ to e_g , respectively. Unfortunately, a specific transition cannot be assigned in this case due to the probable mixed valence state of the cobalt species (see below). The gap between the edges results from the spin–orbit splitting of the $2p$ core hole in Co [40]. The shape of the spectra consists of several different features labelled A–F, which are the result of the Coulomb or exchange interactions between the $3d$ electrons, and these features are clearly seen in all Co-doped SrTiO_3 material spectra. The similarity of the Co $L_{3,2}$ XANES spectra shapes of the doped perovskites and the reference Co_3O_4 oxide indicates that the cobalt possesses a mixed oxidation (+2 and +3) states when it is introduced into the SrTiO_3 crystal lattice. The feature A is present in the CoO spectrum and in the spectra of doped perovskites, indicating the presence of Co^{2+} in the perovskite materials. However, this feature is not seen in the spectrum for Co_3O_4 . The reason is the local symmetry of the cobalt ions: in pure CoO, Co^{2+} ions adopt the high-spin octahedral (O_h) symmetry [41, 42] and in the case of Co_3O_4 , the Co^{2+} ions

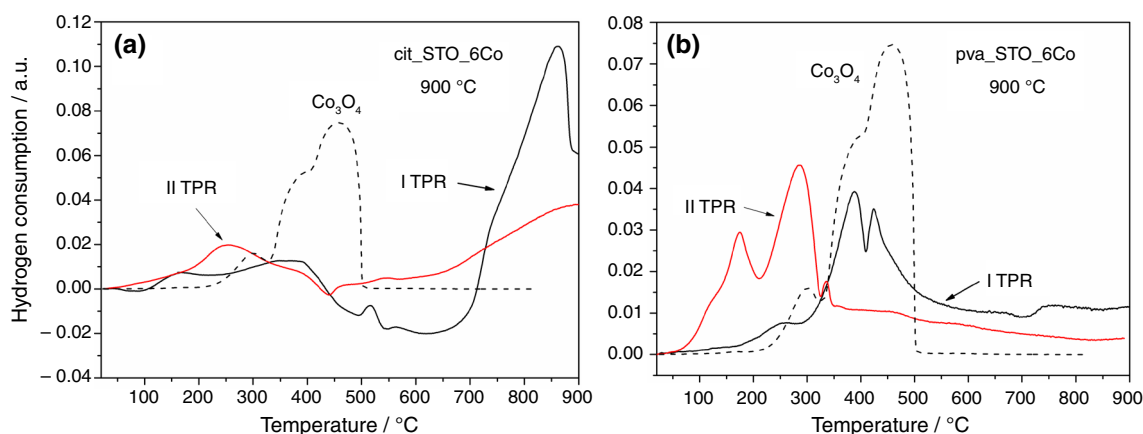


Fig. 7 Comparison of I TPR and II TPR cycle for **a** SrTi_{0.94}Co_{0.06}O₃ from citrate-combustion method and **b** modified Pechini method. The TPR profile of Co₃O₄ reduction was added to each graph

are found in the tetrahedral (T_d) coordination, and the Co³⁺ ions adopt the octahedral coordination [43] which allows us to state that the A feature is characteristic for the presence of the Co²⁺ ions in the octahedral coordination. The presence of the A absorption peak in the spectra registered for the doped perovskites can be a sign of the presence of additional CoO phase in the materials or can be a result of the incorporation of the cobalt in the +2 oxidation state in the Ti positions in strontium titanate (since the titanium in SrTiO₃ also adopts the octahedral symmetry in the TiO₆ octahedron). The second possibility is supported by the fact that excessive cobalt should rather be in the form of the more stable cobalt(II,III) oxide Co₃O₄ after calcination at 700 °C in an air atmosphere. Additionally, we did not observe the CoO phase in the final materials (traces of CoO were only observed in HT-XRD measurements). Considering the A, B, and E absorption peaks, we can observe that the intensities of the signals are increasing in order (2Co, 10Co, and 6Co). Although we did not measure the reference for the +3 Co oxidation state, we can assume the signal from Co²⁺ should have a higher impact on the intensities at these points on the spectrum. The intensities of the features D and F, on the other hand, increase as the cobalt admixture content increases (2Co, 6Co, and 10Co). The absorption peaks of D and F, on the other hand, should be more sensitive to the Co³⁺ valence state than the Co²⁺. Based on the foregoing, we can conclude that cobalt is introduced into the system in both +2 and +3 oxidation states, but when small amounts of cobalt are introduced, the cobalt ions adopt a more +2 oxidation state. When more cobalt is added to SrTiO₃ (10Co), the opposite effect is observed, with a higher fraction of cobalt ions adopting the +3 oxidation state.

The variety of forms in which cobalt occurs in the tested materials was confirmed by the complex profiles of temperature-programmed reduction (TPR). The

temperature-programmed reduction measurements provide information on the ability of the materials to undergo reduction reactions. As mentioned earlier, the reduction and oxidation cycles were alternately performed in the following order: I TPR, I TPOx, and II TPR. The comparison of the I and II TPR cycles for SrTi_{0.94}Co_{0.06}O₃ samples derived from the citrate method and synthesis with the addition of PVA is shown in Fig. 7 as an example for both series of materials. Similar changes in I TPR and II TPR profiles were observed for samples with other compositions.

The shape and the temperature of the peak maxima for both TPR cycles differ in both series (Pechini and citrate methods). However, in the case of cit_STO_6Co, the differences relate primarily to the temperatures of maxima, while in the case of pva_STO_6Co, they are mainly related to the shape of the peaks. Such obvious changes in TPR profiles for the same material testify to the continuous reconstruction of the system and, at the same time, confirm the observations presented on the basis of diffractometric measurements, which indicate a very large influence of the method of annealing the materials on their chemical composition. The graphs also show the II TPR curve for cobalt(II,III) oxide powders (dashed line) obtained by the citric acid method as Co₃O₄ pattern. The TPR profiles for citrate-method materials (Fig. 7a) can be divided into two temperature ranges: the first one—from RT to around 550 °C and the second one—from around 550 °C to 900 °C. Both of these ranges are composed of several reduction peaks, regardless of Co share. However, the shown peaks are asymmetric, which indicates that reduction reactions are multi-step and complex. Such differences in the shape and maximum temperatures of the I and II TPR profiles also mean, that the reduction of the samples is not reversible, i.e., that the material after the first reduction and subsequent oxidation does not return to its original form (before the I TPR cycle). In the first temperature range, two

or three broad reduction peaks occur (both on the I TPR and II TPR profiles), and the reduction begins at a lower temperature compared to the pure Co_3O_4 . It suggests the presence of some cobalt oxides (not necessarily Co_3O_4 , Co_2O_3 or CoO because cobalt also forms non-stoichiometric oxides) in the materials, between the grains, or covering the grains of tausonite, despite their absence in the XRD method results. Moreover, the lack of cobalt-originated phases may indirectly indicate the incorporation of cobalt into the structure of SrTiO_3 . The breadth of peaks below 500 °C with low intensity at the same time can be a result of the multistep and complex mechanism of Co_3O_4 or/and CoO phase reduction. Moreover, the multiplicity of crystalline phases implies different sets of interactions between the cobalt oxides and the supports on which they are located [44]. Thus, these cobalt oxides can undergo reduction reactions more easily or harder. Broad reduction peaks occur in both the I and II TPR cycles in the temperature range above around 450 °C. Most likely, this effect is associated with the reduction of cobalt incorporated into SrTiO_3 and possibly into R-P phase structures or other cobalt-containing phases. Although we didn't observe additional crystal phases with cobalt (CoO , CoO_{1+x} , Co_2O_3 , Co_3O_4 or other Co-containing phases) on diffractograms after calcination, they can be formed during heat treatment on the synthesis stage (as indicated by HT_XRD measurements) and can also be reduced during the TPR cycle [45, 46]. As can be seen, the main difference between the first and second TPR cycles (I TPR and II TPR profiles) in the case of materials from citrate synthesis is much lower maximum above 700 °C on the II TPR profile than the maximum of the I TPR profile (Fig. 7a). This effect is most likely related to the thermal decomposition of SrCO_3 and CO_2 release, as carbonate was present in the materials from the citrate method. The decrease in the area of this reduction peak for the II TPR proves that the carbonate undergoes thermal decomposition in subsequent cycles. For samples obtained from synthesis with PVA, I TPR and II TPR profiles have a similar shape, and the main difference is the temperature shift towards lower temperatures in the case of II TPR profiles compared to the I TPR profile (Fig. 7b). The first reduction peak on the I TPR profile begins at c.a. 200 °C, while in the case of the II TPR profile, the reduction starts below 100 °C (~70 °C). The same shift towards lower temperatures was also registered for samples calcined at 700 °C and 800 °C (not already shown in this manuscript). The similarity of the shape of pva_STO_Co series TPR profiles (for I TPR and II TPR) compared to TPR profiles of cit_STO_xCo series in the high temperature range is a result of single-phase system composition, since the presence of only SrTiO_3 phase in materials synthesized with PVA was indicated. The temperature range of the reduction of the pva_STO_6Co sample (from I TPR) and pure Co_3O_4 overlap may be explained by the reduction of surface layers

of cobalt oxides, which were not detected by the diffraction method but were most likely present in the material, as can be suspected based on XAS tests.. Furthermore, it is primarily because TPR studies indicate the presence of some amounts of cobalt oxides (beyond the level of XRD detection) in pva_STO_Co materials. Additionally, as mentioned before, we observe that the reduction of the material occurs at lower temperatures during the II TPR than during the I TPR. This effect can be a result of the interaction between cobalt oxides and Co-doped SrTiO_3 phase. A similar effect was observed, for example, for nickel-based catalysts deposited on SiO_2 or ZrO_2 supports [47, 48].

In subsequent considerations, only the II TPR cycle results were used to compare samples from the two synthesis methods and within the series. We assumed that the first reduction cycle and the subsequent oxidation cycle would serve as standardisation stages for the measurement.

The II TPR profiles of materials with varying amounts of Co admixture from the citrate method and the PVA-involving method were collected and compared (Fig. 8). In both synthesis routes, we see an increase in the intensity of hydrogen consumption as the Co admixture share increases. In the case of citrate-combustion synthesis samples, the first range of reduction up to 500 °C can be associated with surface Co_3O_4 reduction (Fig. 8a). The overlapping of the reduction temperatures of the Co-doped perovskite materials and the reduction temperatures of pure Co_3O_4 (reference sample) may support this fact. Although the XRD method did not confirm the presence of cobalt oxide as a separate crystal phase, it can take an amorphous form or be present in the materials in small quantities, below the detection level of the XRD method. As previously stated, cobalt reduction in various oxidation states can also occur in the second reduction range (500–900 °C). Given that the intensity of the signal in the II TPR cycle increases with increasing Co content while the proportion of SrTiO_3 , R-P phases, rutile, and SrCO_3 remains constant (Table 1), the concept of reducing cobalt from different crystal structures appears acceptable. The temperature-programmed reduction profiles of the modified Pechini synthesis samples differ from the profiles of the citrate synthesis samples (Fig. 8b, c, d). For all calcination temperatures, the reduction begins below 100 °C for the samples with the lowest Co content (pva_STO_2Co). There are also additional reduction peaks at around 200 and 300 °C. When the calcination temperature rises, the highest reduction peak maxima shift to higher temperatures—330, 350, and 380 °C (for samples calcined at 700, 800, and 900 °C, respectively). For pva_STO_6Co and pva_STO_10Co samples, increasing the calcination temperature results in more complex TPR profiles and separated reduction peaks. The calcination at 700 °C yields the simplest reduction profile, with a possibly doubled reduction peak with a maximum at 250 °C and the broadest reduction range between 400 and 900 °C.

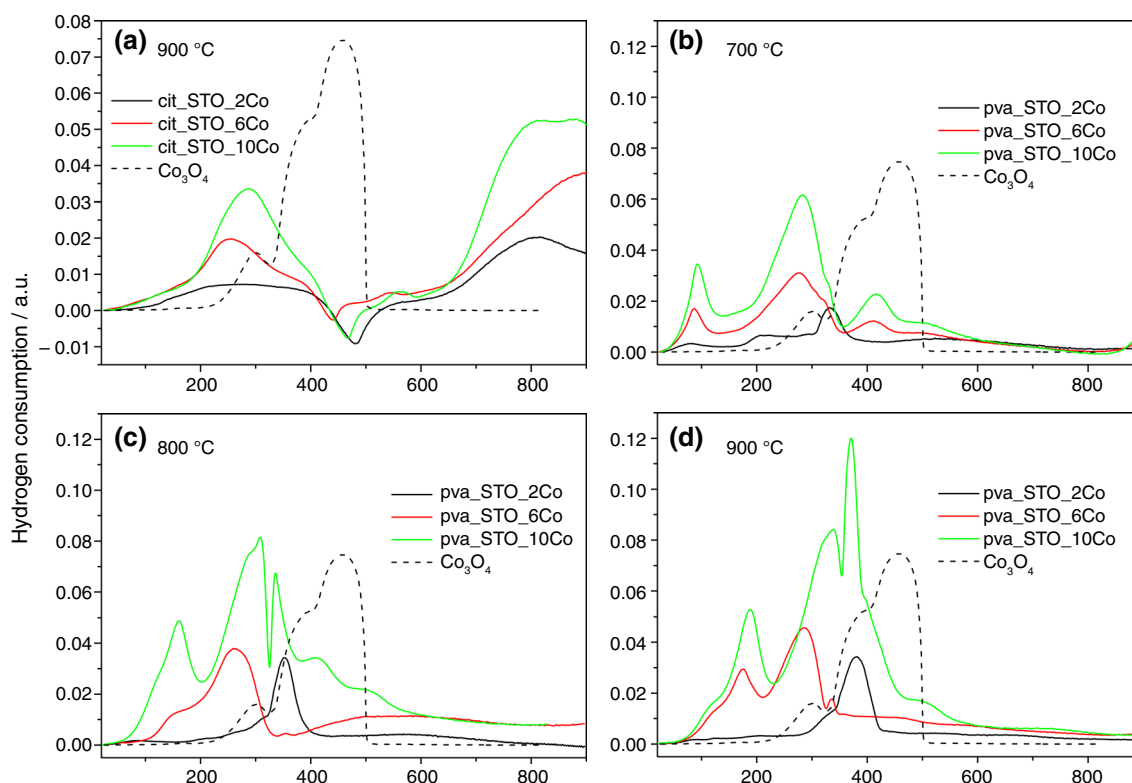


Fig. 8 The comparison of TPR profiles for **a** cit_STO_xCo materials calcinated at 900 °C, **b** pva_STO_xCo materials calcinated at 700 °C, **c** pva_STO_xCo materials calcinated at 800 °C and **d** pva_STO_xCo materials calcinated at 900 °C

For the same chemical composition but a higher calcination temperature (800 °C), there is an additional peak at 150 °C and a similar broad reduction range between 370 and 850 °C. The perovskite materials calcined at 900 °C had the most complex TPR profile, with several reduction peaks. These reduction peaks have a maximum at the following temperatures: 115 °C, 170 °C, 285 °C, 336 °C, and most likely around 460 °C. All these reducing effects are related to the processes of cobalt reduction in various forms (oxide and mixed oxides), in which it is additionally in two different oxidation states. As the calcination temperature rises, one can see the effect of shifting the TPR profile to higher temperatures, which is a consequence of the growth of crystallites (decrease in the amount of fine particles) as a result of their existence at higher temperatures. Because HT XRD and XAS studies indicate that materials in the PVA series may contain cobalt oxides, even if they are not visible in the diffraction patterns of the materials after calcination (Fig. 4), cobalt oxides should be assumed to be present in the pva_STO_xCo series. It can also be seen that the number of reduction peaks obtained for materials with both methods is comparable for samples doped with 10% Co. However, obviously, when pva_STO_xCo samples are calcined at 700 °C, some of the peaks are less distinct than after calcination at higher temperatures. The reducibility of oxides is affected

by a number of factors, including dispersion, the interaction of reducible oxides with their supports, and the degree of crystallinity. Probably the weaker separation of the reduction peaks in the case of materials from lower calcination temperatures is related to the presence of larger amounts of amorphous phases compared to materials calcined at higher temperatures.

From the materials obtained by both methods, pellets were also formed, sintered at 1200 °C, and then tested analogously to the powders after calcination. According to XRD analysis (Table 4), all materials obtained by the PVA method are single-phase (tausonite phase), whereas materials obtained by the citrate method contain (in addition to tausonite as the majority phase), R-P phases, and strontium cobaltate. The amount of SrCoO₃ in the cit_STO_xCo series increases as cobalt is introduced into the system. SrCoO₃ has the same perovskite cubic structure as SrTiO₃ and the same space group (Pm-3 m) as tausonite phase. The cobaltane phase was not present in the materials after calcination, so it was formed only during sintering as a result of ion diffusion in the solid.

The results of the diffractometric measurements were also used to calculate the lattice parameter of the tausonite phase for the materials sintered at 1200 °C using the Rietveld method (Table 5). The analysis was carried out on both,

Table 4 The phase composition of the samples after sintering at 1200 °C

Cobalt amount/mol%	Composition/mas. %	
	cit_STO_xCo	pva_STO_xCo
2	Tausonite 87.5 R-P 6.3 Sr ₂ Co ₂ O ₅ 6.2	Tausonite 100
6	Tausonite 83.9 R-P 7.9 Sr ₂ Co ₂ O ₅ 8.2	Tausonite 100
10	Tausonite 79.1 R-P 11.2 Sr ₂ Co ₂ O ₅ 9.7	Tausonite 100

Table 5 The comparison of lattice parameters of tausonite for sintered samples from both series

Cobalt amount/mol%	Lattice parameter of tausonite phase/Å	
	cit_STO_xCo	pva_STO_xCo
0	3.8941 ± 0.0002	3.8944 ± 0.0002
2	3.9034 ± 0.0004	3.9022 ± 0.0003
6	3.9014 ± 0.0004	3.8988 ± 0.0002
10	3.8977 ± 0.0004	3.8957 ± 0.0003

doped and undoped materials, which were also synthesized using the PVA method and the citrate method. The lattice parameter value for undoped SrTiO₃ is the same regardless of the method used to obtain it (taking into account the error in determining these values). However, the addition of cobalt as an admixture caused significant changes in the value of the lattice parameter of tausonite in both series of materials.

It can be seen that incorporation of 2 mol% of cobalt leads to a significant increase in the value of the lattice parameter in both series of materials, while further increasing the amount of the admixture results in a gradual decrease in this value. Furthermore, all these values are significantly higher than the values of parameters for undoped samples. The increase in the value of the lattice parameter of the tausonite phase for all cobalt-doped samples compared to the value of this parameter for undoped samples proves that cobalt is incorporated into the SrTiO₃ structure. Moreover, it can be seen that the impact of Co amount on lattice parameter is greater for cit_STO_xCo materials. The comparison of the values of titanium and cobalt ionic radii in the sixfold coordination (characteristic for the B element in the ABO₃ perovskite structure) allows for the verification of the hypothesis about the possibility of substituting titanium with cobalt in strontium titanate. In the form of Ti⁴⁺, in which titanium is in SrTiO₃, ionic radii are 0.745 Å [49]. The values of ionic radii for cobalt depend on the Co oxidation state in the SrTiO₃ structure, as cobalt can exist in four

different oxidation states: Co²⁺, Co³⁺, and Co⁴⁺. Moreover, in the first (+2) and the second (+3) cases, two configurations are possible: low and high spin, for which the ionic radii values are also different. Thus, these values of ionic radii are: Co²⁺—0.790 Å—for low spin configuration and 0.885 Å for high spin configuration; Co³⁺—0.685 Å—for low spin configuration and 0.75 Å for high spin configuration, and Co⁴⁺—0.67 Å for high spin configuration. On the basis of these values, it can be concluded that incorporation of cobalt in the +2 oxidation state should result in an increase of SrTiO₃ lattice parameter, while incorporation of cobalt in the +3, and/or above all, +4 oxidation state should decrease the lattice parameter value. Thus, adding small amounts of cobalt will most likely lead to the incorporation of Co on +2 oxidation state, while the more Co is introduced into the structure, the more often it will take a higher, +3 or/and +4) oxidation state. A similar effect has already been observed during the study of SrTiO₃ system with introduced nickel [50]. Additionally, XAS test results for pva_STO_xCo series materials presented in the section on materials after calcination also indicated a change in the oxidation state of cobalt from +2 to +3 along with its increased amount in the material. It should be noted, however, that in the case of materials after calcination, cobalt can be incorporated into the structure of tausonite in a different form (with a different oxidation state) than in the case of materials after sintering at 1200 °C. Moreover, with increasing temperature, the probability of lattice defects and reactions between individual oxides increases, as evidenced, i.e., by the formation of cobaltate phases.

TPR profiles of sintered materials (Fig. 9) not only differ in shape but also in peak temperatures compared to TPR profiles of materials after calcination, both in the case of measurements made for materials from the PVA series and from the citrate series. First of all, the TPR profiles of the sinters show a shift in the reduction effects towards higher temperatures compared to the profiles for powders after calcination. This effect is the result of the grains growing and fusing under the influence of temperature, and thus also the reduction of the amount of nanograins (or nanocrystallites), which are always the first to be reduced. Moreover, increasing the temperature of thermal treatment may result in the introduction of some cobalt bound in simple oxides (at the calcination stage) into the SrTiO₃ structure during sintering. Unfortunately, the assignment of the peaks to specific reduction processes (reduction oxides or doped-SrTiO₃ phases) is not possible, although the TPR profiles of the materials after sintering seem to be of a less complicated nature.

Both the comparison of the phase composition and TPR profiles of the materials based on cobalt-doped strontium titanate obtained with the two seemingly slightly different methods (with the use of PVA and the citrate method) indicate that the materials obtained by these methods differ

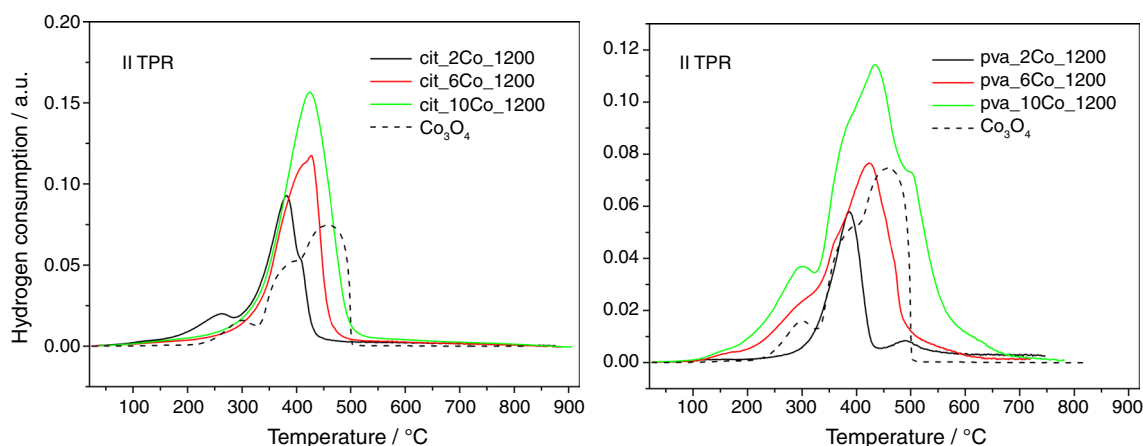
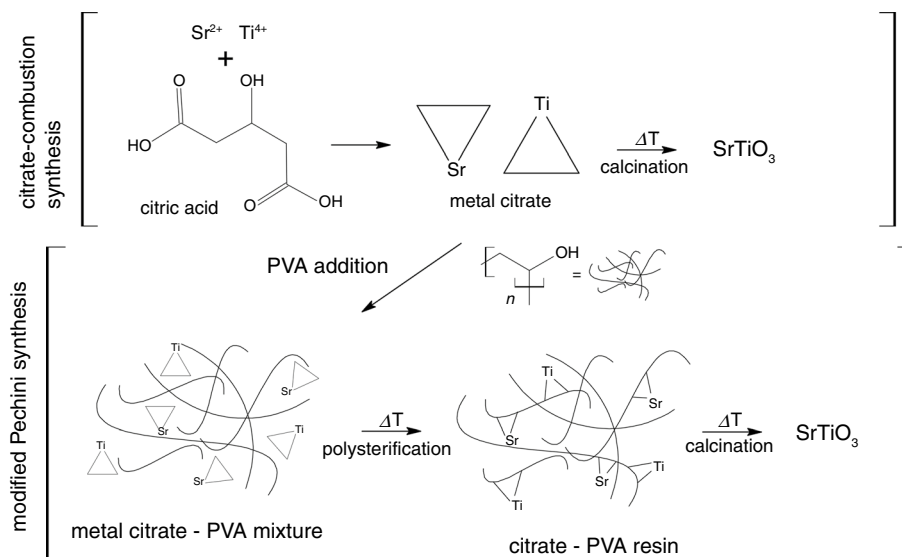


Fig. 9 Comparison of II TPR profiles registered for sintered materials synthesized using **a** citrate combustion method and **b** the modified Pechini method

Fig. 10 The two synthesis routes for strontium titanate are depicted schematically (without Co to make the picture more clear). The modified Pechini synthesis begins in the same way as the citrate-combustion synthesis (preparation of metal–citrate complexes). In the classic Pechini synthesis, which is also described in the paper, ethylene glycol is typically used instead of the PVA polymer



significantly from each other. The materials obtained using PVA are more homogeneous in terms of phase composition compared to the materials obtained by the citrate method. However, this does not result in a lesser degree of complication of the TPR profiles of the pva_xCo_STO series, as in these materials, in addition to the cobalt incorporated in the perovskite structure, the presence of cobalt oxide (CoO) can be suspected. It can be seen that only in the case of the pva_STO₂Co material does the first low-temperature reduction peak not appear on the TPR profile, which may indicate that it is the only single-phase material in which all the cobalt present is incorporated into the tausonite structure.

To sum up, the materials obtained by both methods, both in terms of powders after calcination and materials after 1200 °C, differ primarily in phase composition, which affects the susceptibility to reduction processes occurring in these

materials. The comparison of the processes taking place during the synthesis of materials with both methods shows that the materials obtained by the PVA method (i.e., the modified Pechini method) are phase homogeneous because metals trapped in the polymer network do not segregate in the form of separate oxides and carbonates during thermal processing. In such a case (with PVA), the polyesterification reaction takes place between the hydroxyl groups of the polymer and the carboxyl groups of citrates. The application of PVA was previously used for the synthesis of metal oxides, and usually it requires less PVA addition than in the classic Pechini method. The scheme of synthesis was presented below in the form of a diagram (Fig. 10), which describes the sequence of processes taking place in the case of both PVA and the citrate method used in our research.

Conclusions

To obtain Co-doped SrTiO_3 materials, two wet chemical synthesis methods (citrate-combustion synthesis and modified Pechini synthesis) were applied. From both methods, mixed oxide perovskite materials were produced. However, XRD measurements show that using the modified Pechini method, a more homogeneous final ceramic powder can be obtained compared to the citrate-combustion method, for which the presence of TiO_2 , SrCO_3 , and Ruddlesden-Popper phases was observed (besides the SrTiO_3 crystal phase). TG measurements allowed to estimate the materials' minimum calcination temperature at 900 °C and 700 °C for the citrate-combustion series and the modified Pechini series, respectively.

The XAS measurements for samples from the PVA synthesis confirmed that cobalt exists in the perovskite material in both +2 and +3 oxidation states. Moreover, it can be stated that the ratio of $\text{Co}^{2+}/\text{Co}^{3+}$ ions in the tausonite crystal lattice is affected by the amount of cobalt introduced during the precursor mixing stage of the synthesis. The ratio will be greater in samples with a low amount of cobalt introduced (e.g., pva_STO_2Co) and decrease with an increasing amount of cobalt introduced during synthesis (pva_STO_10Co).

TPR/TPOx measurements show the main differences between the I TPR and II TPR cycles, including the lower intensity of the hydrogen consumption in II TPR above 700 °C in the case of the citrate method (as a result of SrCO_3 decomposition) and the shift of the reduction peaks towards lower temperatures (of about 70 °C) in the case of the modified Pechini method (as a result of interaction between cobalt oxides and Co-doped SrTiO_3 phase). The reduction profiles are generally more complex for the samples from Pechini synthesis, despite the fact that these materials are more homogeneous in terms of phase composition. This may be a result of the presence of cobalt in these materials at different oxidation states (confirmed by XAS tests).

The increase in the calcination temperature in the case of samples with PVA results in a shift of the reduction profiles towards higher temperatures, corresponding with the harder reduction of the materials whose grains grow during the heating at 800 and 900 °C (compared to the series calcined at 700 °C).

The SrTiO_3 lattice parameter changes of the Co-doped SrTiO_3 materials sintered at 1200 °C are in agreement with the results from the XAS experiment, since the change of the lattice parameter of tausonite confirms that in the sample with lower cobalt content, the fraction of Co^{2+} is higher than in the sample with higher cobalt content. The diffraction tests were carried out for the sinters of both series,

and a similar tendency for lattice parameter changes was observed in both series. This behaviour is due to the following dependencies: the fraction of Co^{2+} is higher in the sample with a lower cobalt content as the Co^{2+} ionic radii are larger than the ionic radii of Ti^{4+} , and for the sample with a higher cobalt content, the $\text{Co}^{2+}/\text{Co}^{3+}$ ratio decreases as the ionic radii of Co^{3+} are lower than the Ti^{4+} ionic radii.

XRD and TPR measurements revealed that the use of two slightly different wet chemical synthesis methods results in the production of materials that are substantially different from one another.

Acknowledgements AM has been partly supported by the EU Project POWR.03.02.00-00-I004/16. This publication was developed under the provision of the Polish Ministry of Education and Science project: "Support for research and development with the use of research infrastructure of the National Synchrotron Radiation Centre SOLARIS" under contract nr 1/SOL/2021/2. We acknowledge SOLARIS Centre for the access to the Beamline PIRX, where the measurements were performed.

Author contributions Conceptualization: AM and ED; methodology: ED; formal analysis and investigation: AM and ED; writing—original draft preparation: AM and ED; funding acquisition: AM; resources: AM, supervision: ED. All authors read and approved the final manuscript.

Declarations

Conflict of interest The authors declare that they have no known competing financial interests or personal relationships that could have appeared to influence the work reported in this paper.

Open Access This article is licensed under a Creative Commons Attribution 4.0 International License, which permits use, sharing, adaptation, distribution and reproduction in any medium or format, as long as you give appropriate credit to the original author(s) and the source, provide a link to the Creative Commons licence, and indicate if changes were made. The images or other third party material in this article are included in the article's Creative Commons licence, unless indicated otherwise in a credit line to the material. If material is not included in the article's Creative Commons licence and your intended use is not permitted by statutory regulation or exceeds the permitted use, you will need to obtain permission directly from the copyright holder. To view a copy of this licence, visit <http://creativecommons.org/licenses/by/4.0/>.

References

1. Euvrard J, Yan Y, Mitzi DB. Electrical doping in halide perovskites. *Nat Rev Mater.* 2021;6:531–49. <https://doi.org/10.1038/s41578-021-00286-z>.
2. Mizera A, Kowalczyk A, Chmielarz L, Drożdż E. Catalysts based on strontium titanate doped with Ni/Co/Cu for dry reforming of methane. *Materials.* 2021;14:7227. <https://doi.org/10.3390/MA14237227>.
3. Djellabi R, Ordóñez MF, Conte F, et al. A review of advances in multifunctional XTiO_3 perovskite-type oxides as piezo-photocatalysts for environmental remediation and energy production. *J Hazard Mater.* 2022;421:126792. <https://doi.org/10.1016/J.JHAZMAT.2021.126792>.
4. Longo V, Leick N, Roozeboom F, et al. Structure, magnetic properties and magnetoelastic anisotropy in epitaxial $\text{Sr}(\text{Ti}_{1-x}\text{Co}_x)\text{O}_3$

- films. *New J Phys.* 2010;12:043044. <https://doi.org/10.1088/1367-2630/12/4/043044>.
5. Posadas AB, Mitra C, Lin C, et al. Oxygen vacancy-mediated room-temperature ferromagnetism in insulating cobalt-substituted SrTiO₃ epitaxially integrated with silicon. *Phys Rev B.* 2013;87:144422. <https://doi.org/10.1103/PhysRevB.87.144422>.
6. Pascanut C, Dragoe N, Berthet P. Magnetic and transport properties of cobalt-doped perovskites SrTi_{1-x}Co_xO₃ (x ≤ 0.5). *J Magn Magn Mater.* 2006;305:6–11. <https://doi.org/10.1016/J.JMMM.2005.11.020>.
7. Malo S, Maignan A. Structural, magnetic, and transport properties of the SrTi_{1-x}Co_xO_{3-δ} perovskite (0 ≤ x ≤ 0.9). *Inorg Chem.* 2004;43:8169–75. <https://doi.org/10.1021/ic0490371>.
8. Kim DH, Bi L, Jiang P, et al. Magnetoelastic effects in SrTi_{1-x}M_xO₃ (M=Fe Co, or Cr) epitaxial thin films. *Phys Rev B.* 2011;84:014416. <https://doi.org/10.1103/PhysRevB.84.014416>.
9. Yao D, Zhou X, Ge S. Raman scattering and room temperature ferromagnetism in Co-doped SrTiO₃ particles. *Appl Surf Sci.* 2011;257:9233–6. <https://doi.org/10.1016/j.apsusc.2011.04.039>.
10. Murashkina A, Maragou V, Medvedev D, et al. Single phase materials based on Co-doped SrTiO₃ for mixed ionic-electronic conductors applications. *J Power Sources.* 2012;210:339–44. <https://doi.org/10.1016/j.jpowsour.2012.02.066>.
11. Hui S, Petric A. Electrical conductivity of yttrium-doped SrTiO₃: influence of transition metal additives. *Mater Res Bull.* 2023;37:1215–31. [https://doi.org/10.1016/S0025-5408\(02\)00774-2](https://doi.org/10.1016/S0025-5408(02)00774-2).
12. Ichihara F, Murata Y, Ono H, et al. Characterization of SrTiO₃ target doped with Co ions, SrCo_xTi_{1-x}O_{3-δ}, and their thin films prepared by pulsed laser ablation (PLA) in water for visible light response. *Appl Surf Sci.* 2017;419:126–37. <https://doi.org/10.1016/J.APSUSC.2017.04.130>.
13. Yoshiyama Y, Hosokawa S, Asakura H, et al. Oxygen storage capacity of Co-doped SrTiO₃ with high redox performance. *J Phys Chem C.* 2022;126:4415–22. <https://doi.org/10.1021/acs.jpcc.1c10693>.
14. Glisenti A, Natile MM, Carlotto S, Vittadini A. Co- and Cu-doped titanates: toward a new generation of catalytic converters. *Catal Lett.* 2014;144:1466–71. <https://doi.org/10.1007/S10562-014-1294-5>.
15. Carlotto S, Natile MM, Glisenti A, Vittadini A. Adsorption of small molecules at the cobalt-doped SrTiO₃(001) surface: a first-principles investigation. *Surf Sci.* 2015;633:68–76. <https://doi.org/10.1016/J.SUSC.2014.11.025>.
16. Carlotto S, Natile MM, Glisenti A, Vittadini A. Catalytic mechanisms of NO reduction in a CO–NO atmosphere at Co- and Cu-doped SrTiO₃(100) surfaces. *J Phys Chem C.* 2018;122:449–54. <https://doi.org/10.1021/acs.jpcc.7b09279>.
17. Danks AE, Hall SR, Schnepf Z. The evolution of ‘sol–gel’ chemistry as a technique for materials synthesis. *Mater Horiz.* 2016;3:91–112. <https://doi.org/10.1039/C5MH00260E>.
18. Nikam AV, Prasad BLV, Kulkarni AA. Wet chemical synthesis of metal oxide nanoparticles: a review. *CrystEngComm.* 2018;20:5091–107. <https://doi.org/10.1039/C8CE00487K>.
19. Senthilkumar C, Shashikanth FW. Room temperature weak ferromagnetism in new Bi₂MnCrO₆ synthesized by gel combustion method. *Appl Phys A.* 2022;128:1–8. <https://doi.org/10.1007/S00339-022-05400-8>.
20. Lu J, Li Y, Huang W. Structure and electrical properties of BaCe_{1-x}La_xO_{3-δ} mixed conductors. *Ceram Int.* 2022;48:22476–84. <https://doi.org/10.1016/J.CERAMINT.2022.04.258>.
21. Torres SOA, Rosa JPM, Thomazini D, Gelfuso MV. Thermoelectric properties of CaMnO₃ ceramics produced by using powder synthesized by modified Pechini method. *Process Appl Ceram.* 2022;16:115–24. <https://doi.org/10.2298/PAC2202115T>.
22. Chen R-Y, Zhou D-F, Zhu X-F, et al. A promising Nb-doped La_{0.5}Sr_{0.5}Co_{0.8}Cu_{0.2}O_{3-δ} cathode materials for intermediate temperature solid oxide fuel cells. *J Alloys Compd.* 2022;924:166526. <https://doi.org/10.1016/J.JALLCOM.2022.166526>.
23. Sharmoukh W, Hameed TA, Yakout SM. New nonmagnetic aliovalent dopants (Li⁺, Cu²⁺, In³⁺ and Ti⁴⁺): optical and strong intrinsic room temperature ferromagnetism of perovskite BaSnO₃. *J Alloys Compd.* 2022;925:166702. <https://doi.org/10.1016/J.JALLCOM.2022.166702>.
24. Chen WF, Mofarah SS, Hanaor DAH, et al. Enhancement of Ce/Cr codopant solubility and chemical homogeneity in TiO₂ nanoparticles through sol–gel versus Pechini syntheses. *Inorg Chem.* 2018;57:7279–89. <https://doi.org/10.1021/acs.inorgchem.8b00926>.
25. Rosczyk BR, Lee SJ, Kriven WM. Comparative study of titanate syntheses by the organic steric entrapment method. *Int J Appl Ceram Technol.* 2022;19:200–9. <https://doi.org/10.1111/IJAC.13887>.
26. Taheri SM, Fischer S, Förster S. Routes to nanoparticle-polymer superlattices. *Polymers (Basel).* 2011;3:662–73. <https://doi.org/10.3390/polym3020662>.
27. Ribero D, Kriven WM, Ribero D, Kriven WM. Synthesis of LiFePO₄ powder by the organic-inorganic steric entrapment method. *J Mater Res.* 2013;30:2133–43. <https://doi.org/10.1557/JMR.2015.181>.
28. Ulic R, Tolman K, Chan K, et al. Effective size of vacancies in aliovalently doped SrTiO₃ perovskites. *J Alloys Compd.* 2013;575:239–45. <https://doi.org/10.1016/j.jallcom.2013.04.091>.
29. Ohya Y. Aqueous precursors. In: Klein L, Aparicio M, Jitianu A, editors. *Handbook of sol–gel science and technology*. Cham: Springer; 2017. https://doi.org/10.1007/978-3-319-19454-7_5-1.
30. Edler KJ. Formation of ordered mesoporous thin films through templating. In: Klein L, Aparicio M, Jitianu A, editors. *Handbook of sol–gel science and technology*. Cham: Springer; 2018. https://doi.org/10.1007/978-3-319-32101-1_26.
31. Drożdż E, Łańcucki Ł, Łącz A. Synthesis, microstructural properties and chemical stability of 3DOM structures of Sr_{1-x}Y_xTiO₃. *J Therm Anal Calorim.* 2016;125:1225–31. <https://doi.org/10.1007/S10973-016-5463-1>.
32. Barbooti MM, Al-Sammerrai DA. Thermal decomposition of citric acid. *Thermochim Acta.* 1986;98:119–26. [https://doi.org/10.1016/0040-6031\(86\)87081-2](https://doi.org/10.1016/0040-6031(86)87081-2).
33. Shie JL, Chen YH, Chang CY, et al. Thermal pyrolysis of poly(vinyl alcohol) and its major products. *Energy Fuel.* 2001;16:109–18. <https://doi.org/10.1021/EF010082S>.
34. Ptáček P, Bartoníčková E, Švec J, et al. The kinetics and mechanism of thermal decomposition of SrCO₃ polymorphs. *Ceram Int.* 2015;41:115–26. <https://doi.org/10.1016/J.CERAMINT.2014.08.043>.
35. Mayer NA, Cupid DM, Adam R, et al. Standard enthalpy of reaction for the reduction of Co₃O₄ to CoO. *Thermochim Acta.* 2017;652:109–18. <https://doi.org/10.1016/J.TCA.2017.03.011>.
36. Narducci D, Negroni F, Mari CM. High temperature standard gibbs free energy determinations for Co–o systems by e.m.f. measurements. A statistical approach to evaluate the reliability of the current methods. *Mater Chem Phys.* 1985;12:377–88. [https://doi.org/10.1016/0254-0584\(85\)90107-5](https://doi.org/10.1016/0254-0584(85)90107-5).
37. Wu M, Xin HL, Wang JO, et al. Investigation of the multiplet features of SrTiO₃ in X-ray absorption spectra based on configuration interaction calculations. *J Synchrotron Radiat.* 2018;25:777–84. <https://doi.org/10.1107/S160057751800423X>.
38. Panchal G, Shukla DK, Choudhary RJ, et al. The effect of oxygen stoichiometry at the interface of epitaxial LaTiO₃/La_{0.7}Sr_{0.3}MnO₃ bilayers on its electronic and magnetic properties. *J Appl Phys.* 2017;122:085310. <https://doi.org/10.1063/1.5000133>.

39. de Groot F. Multiplet effects in X-ray spectroscopy. *Coord Chem Rev.* 2005;1–2:31–63. <https://doi.org/10.1016/J.CCR.2004.03.018>.
40. van der Laan G, Kirkman IW. The $2p$ absorption spectra of $3d$ transition metal compounds in tetrahedral and octahedral symmetry. *J Phys Condens Matter.* 1992;4:4189. <https://doi.org/10.1088/0953-8984/4/16/019>.
41. Guan H, Wang X, Li H, et al. CoO octahedral nanocages for high-performance lithium ion batteries. *Chem Commun.* 2012;48:4878–80. <https://doi.org/10.1039/C2CC30843F>.
42. Hibberd AM, Doan HQ, Glass EN, et al. Co polyoxometalates and a Co_3O_4 thin film investigated by L-edge X-ray absorption spectroscopy. *J Phys Chem.* 2015;119:4173–9. <https://doi.org/10.1021/jp5124037>.
43. Osakoo N, Henkel R, Loiha S, et al. Palladium-promoted cobalt catalysts supported on silica prepared by impregnation and reverse micelle for Fischer–Tropsch synthesis. *Appl Catal A Gen.* 2013;464–465:269–80. <https://doi.org/10.1016/J.APCATA.2013.06.008>.
44. Drożdż E, Łącz A, Spalek Z. Deposition of NiO on 3 mol% yttria-stabilized zirconia and $\text{Sr}_{0.96}\text{Y}_{0.04}\text{TiO}_3$ materials by impregnation method. *J Therm Anal Calorim.* 2017;130:291–9. <https://doi.org/10.1007/S10973-017-6406-1>.
45. James OO, Maity S. Temperature programme reduction (TPR) studies of cobalt phases in γ -alumina supported cobalt catalysts. *J Petrol Technol Altern Fuel.* 1986;7:1–12. <https://doi.org/10.5897/JPTAF2015.0122>.
46. Li C, Wong L, Tang L, et al. Kinetic modelling of temperature-programmed reduction of cobalt oxide by hydrogen. *Appl Catal A Gen.* 2017;537:1–11. <https://doi.org/10.1016/J.APCATA.2017.02.022>.
47. Rossetti I, Biffi C, Bianchi CL, et al. Ni/SiO₂ and Ni/ZrO₂ catalysts for the steam reforming of ethanol. *Appl Catal B.* 2012;117–118:384–96. <https://doi.org/10.1016/J.APCATB.2012.02.006>.
48. Song YQ, He DH, Xu BQ. Effects of preparation methods of ZrO₂ support on catalytic performances of Ni/ZrO₂ catalysts in methane partial oxidation to syngas. *Appl Catal A Gen.* 2008;337:19–28. <https://doi.org/10.1016/J.APCATA.2007.11.032>.
49. Shannon RD. Revised effective ionic radii and systematic studies of interatomic distances in halides and chalcogenides. *Acta Crystallogr A.* 1976;32:751–67. <https://doi.org/10.1107/S0567739476001551>.
50. Mizera A, Drożdż E. Studies on structural, redox and electrical properties of Ni-doped strontium titanate materials. *Ceram Int.* 2020;46:24635–41. <https://doi.org/10.1016/J.CERAMINT.2020.06.252>.

Publisher's Note Springer Nature remains neutral with regard to jurisdictional claims in published maps and institutional affiliations.